JM PAPERS

Predicting initial microlayer thickness in nucleate boiling using Landau–Levich theory

Xiaolong Zhang (张晓龙)[1], Ismail El Mellas[1] and Mirco Magnini[1],†

[1]Faculty of Engineering, University of Nottingham, Nottingham NG7 2QL, UK

A phenomenological model is proposed to estimate the initial thickness of the liquid microlayer forming beneath a vapour bubble growing on a solid surface upon nucleate boiling. The model employs an analogy between the microlayer formation and the classic plate withdrawal problem. It calculates the microlayer thickness by considering it as a Landau–Levich film, where the thickness is a function of the meniscus speed and radius of curvature. Given the nearly hemispherical shape of the bubble during the early growth stage when the microlayer is first deposited, we assume that the meniscus speed can be approximated by the bubble expansion rate, and estimate the meniscus curvature using the Rayleigh equations. Unlike previous theories that assume that the bubble radius growth is proportional to the square root of time, the proposed model does not rely on any specific law of growth for vapour bubbles. The model is validated for predicting the microlayer thickness in water and ethanol, showing good agreement with experimental measurements and empirical correlations. Subsequent analyses of the microlayer interface profile address inconsistent reports – some described a wedge-like shape, whereas others reported a slight outward curvature with decreasing thickness in the outer region. This discrepancy is attributed to a reduction in the expansion rate of the microlayer's outer edge, particularly when the bubble reaches its maximum width. Our model provides insights into microlayer dynamics, essential to boiling heat transfer, as the evaporative heat flux through the microlayer is very sensitive to its initial thickness.

Key words: boiling, thin films, lubrication theory

1. Introduction

The growth of vapour bubbles on heated solid surfaces under conditions of high superheating and low pressure is typically rapid. During this rapid expansion, which occurs

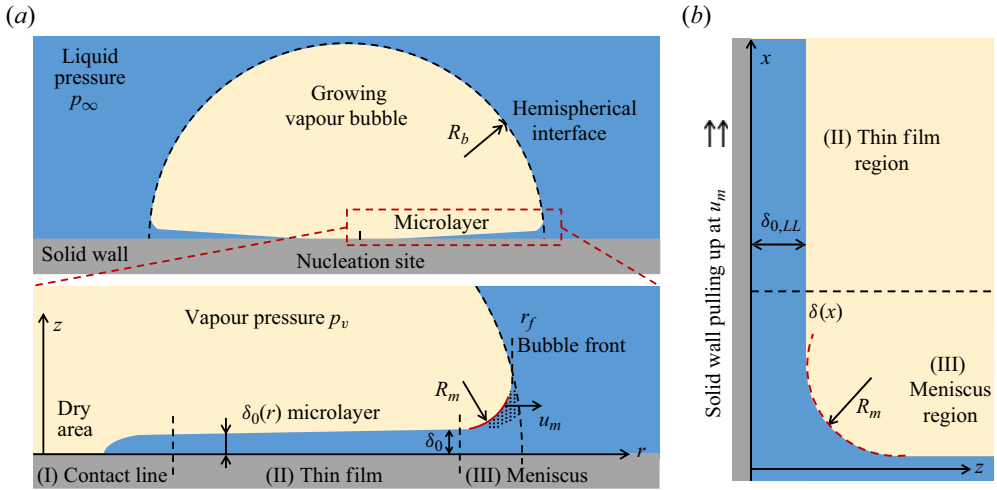† Email address for correspondence: mirco.magnini@nottingham.ac.uk

Figure 1. (*a*) A simplified illustration (not to scale) of a vapour bubble growing on a solid wall; the microlayer beneath the bubble is made thicker to aid visualisation. (*b*) Dragging of a viscous liquid by a moving plate, also known as the Landau–Levich problem.

shortly after the initial formation of a vapour bubble embryo, a thin micrometre-thick liquid layer is often trapped under the bubble on the solid surface (Moore & Mesler 1961; Tong & Tang 2017), as depicted in the schematic in figure 1(*a*). Due to the microlayer's small thickness, heat conducted through it leads to rapid liquid evaporation. As a result, a high local heat transfer coefficient is achieved. Liquid evaporation from the microlayer is believed to make a significant contribution to the volume growth of the vapour bubble and to the high heat transfer performance observed in boiling phenomena (Cooper & Lloyd 1969; Chen *et al.* 2020; Bureš & Sato 2022; Tecchio *et al.* 2022).

The thickness of the microlayer, illustrated in figure 1(*a*), denotes the thickness of the portion of the liquid layer that is trapped under the bubble and away from the bubble front. Experimental observations (Jung & Kim 2014; Sinha, Narayan & Srivastava 2022; Tecchio *et al.* 2022) have indicated that post-formation, the microlayer undergoes thinning due to evaporation, which depends on the initial thickness δ_0 when the microlayer is first created. The term 'initial' refers to the thickness of the microlayer when it is first deposited.

Several models have been proposed to determine the initial thickness of the microlayer. The boundary layer consideration has been a popular approach to determine this value used by researchers (Cooper & Lloyd 1969; Olander & Watts 1969; van Ouwerkerk 1971). As the bubble grows, it pushes the liquid outwards, leading to the development of a laminar boundary layer on the solid surface. The microlayer thickness δ_0 is assumed to be equal to the displacement thickness of this viscous boundary layer. A simple formula (1.1) was first derived by Cooper & Lloyd (1969) based on the assumption that the bubble radius obeys an $R_b \propto t^{1/2}$ law:

$$\delta_0 = C\sqrt{\nu t}, \tag{1.1}$$

where ν is the liquid kinematic viscosity, C is a constant, and t is the growth time since nucleation. Equation (1.1) considers only the kinematic viscosity as a material parameter, and does not include the effect of surface tension, which was recently demonstrated to have an impact on the microlayer thickness (Hänsch & Walker 2016).

The coefficient C has been subject to various estimations. Olander & Watts (1969) proposed $C = \sqrt{\pi}/2$, while Cooper & Lloyd (1969), accounting for short-lived effects

of residual flows near the bubble front, suggested a slightly smaller value, $C \approx 0.8$. Details on the derivation of (1.1) and potential improvements of the underlying model are provided in Appendix A. van Ouwerkerk (1971) adopted a cylindrical geometry and proposed the coefficient $C \approx 1.27$. However, experimental measurements have indicated that this formula tends to overestimate the microlayer thickness. Empirical approaches using experimental data have also been employed to determine C, with reported values such as $C \approx 0.3$–0.4 for water (Koffman & Plesset 1983), and $C \approx 0.22$ for ethanol vapour bubbles (Gao *et al.* 2013).

Additionally, the predictions of (1.1) yield a monotonic increase in the thickness from the nucleation site, whilst recent experiments (Chen, Haginiwa & Utaka 2017; Sinha *et al.* 2022; Tecchio *et al.* 2022) and computational fluid dynamics simulations (Hänsch & Walker 2019) have revealed more complex liquid film profiles. A non-monotonic behaviour was observed, where the microlayer thickness initially increases, reaches a maximum and then decreases in its outermost part. This profile evolution was not explained by traditional boundary-layer approaches. The proportionality law of $R_b \propto t^{0.5}$ was originally derived to describe the heat-transfer-controlled growth of bubbles in a uniformly superheated liquid (Plesset & Zwick 1954; Mikic, Rohsenow & Griffith 1970). However, the validity of this law is questionable in practical situations where bubbles form upon heterogeneous nucleation on a heated wall and grow in a liquid with a non-uniform temperature.

A different approach was adopted by Smirnov (1975), who conducted a hydrodynamic analysis of the liquid flow near the bubble front and in the microlayer, assuming a two-dimensional axisymmetric radial flow. The formula that he proposed to calculate the microlayer thickness is

$$\delta_0 = \sqrt{\frac{2\nu \dot{R}_b}{-9\ddot{R}_b - \dfrac{2R_b \dddot{R}_b}{\dot{R}_b} + \dfrac{2\dot{R}_b^2}{3R_b}}}, \tag{1.2}$$

where R_b is the bubble radius, and a dot over a quantity indicates its time derivative. Equation (1.2) does not depend on any specific bubble growth law. Upon a meticulous examination of the derivation, we identified flawed physical assumptions that raise concerns about the formula's validity. Detailed information is provided in Appendix B. Nevertheless, his approach has enlightening aspects, such as that the microlayer formation should be viewed as a local phenomenon linked to the liquid flow near the bubble front, rather than relating it to the liquid boundary layer outside the bubble as in the previous theories.

Katto & Shoji (1970) argued that microlayer formation is intricately related to the flow of viscous liquid near the front of the bubble. This flow is driven by the pressure drop resulting from surface tension and changes in the curvature of the free interface. Zijl & Moalem-Maron (1978) were the first to hypothesise that the physical origin for microlayer formation is analogous to the thin liquid film deposited on a solid plate when it is withdrawn vertically from a liquid bath. This problem, famously known as the Landau–Levich film problem (Landau & Levich 1942), offers useful insights into the microlayer formation mechanism.

Zijl & Moalem-Maron (1978) regarded the outward expanding bubble front as the meniscus formed in the Landau–Levich problem upon the free liquid surface, and estimated the microlayer thickness as

$$\delta_0 = 0.944 \sqrt{2} \left(\frac{\mu u_m}{\sigma} \right)^{2/3} R_m, \tag{1.3}$$

with μ being the liquid dynamic viscosity, σ the surface tension, u_m the speed of the bubble front, and R_m the meniscus radius of curvature (see figure 1a). The latter was calculated via a modified expression of the capillary length where the meniscus acceleration replaced the gravitation acceleration:

$$R_m = \frac{1}{2}\left(-\frac{2\sigma}{\rho\ddot{R}_b}\right)^{1/2}, \tag{1.4}$$

where ρ is the liquid density. However, this line of thought was largely overlooked and did not gain popularity in microlayer studies.

Recently, Tecchio *et al.* (2022) revisited the Landau–Levich film to explain the outward-curved interface profile of the microlayer observed in their experiments. They hypothesised that the microlayer could be regarded as a liquid film deposited by the expansion of the bubble front. The decrease in the microlayer thickness was attributed to the reduction in the bubble expansion rate at the later growth stage. It was the first time a physical origin was provided for the non-monotonic profile, as the traditional boundary layer approach failed to do so. The value of R_m was determined from their experimental data. Kim & Seok Oh (2021) also used (1.3) for predicting the initial microlayer thickness; however, they do not address the non-monotonic profile observed in experiments (Chen *et al.* 2017; Utaka *et al.* 2018).

This study proposes a simple model for predicting the initial thickness of the microlayer. This prediction is grounded on a phenomenological comparison between the microlayer and the Landau–Levich film. The term 'initial' emphasises the pure hydrodynamic aspect of the problem, concentrating on the microlayer thickness immediately upon its formation. Therefore, microlayer thinning resulting from evaporation after its creation is not accounted for. For validation, we undertake a comparative study between the model predictions and experimental data, examining various bubble growth laws for both water and ethanol. A noteworthy feature of our model is that it is free from empirical constants. Subsequently, we use the model to address and explain contrasting experimental observations about the interface profile of the microlayer.

2. Problem formulation

We consider the axisymmetric growth of a vapour bubble on a flat smooth surface submerged in a large pool of liquid, as illustrated in figure 1(a). A two-dimensional axisymmetric reference frame (r, z) centred on the nucleation site is adopted, with z indicating the vertical (axial) direction, and r the horizontal (radial) direction. At a specific time moment t_i, the outer edge of the microlayer has reached the radial position r_i, located around the border of regions (II) and (III) in figure 1(a), with local thickness denoted as δ_0. By collecting a series of δ_0 values at different r_i as time elapses, we can construct the initial thickness profile of the microlayer as a function of r, resulting in $\delta_0(r)$. The microlayer interface remains static once the microlayer is deposited on the solid without phase change or contact line motion (Zhang, El Mellas & Magnini 2024). Hence the interface profile of the microlayer located on the left-hand side of the end of the microlayer ($r < r_i$) is the initial thickness of the microlayer, $\delta_0(r)$, depicted in figure 1(a), deposited before this instant t_i.

We investigate the rapid volumetric growth of the bubble. In reality, this phenomenon is observed in situations with high wall superheats, high wall heat fluxes, and low system pressures (Carey 2020). The rapid growth pattern results in the bubble taking a nearly hemispherical shape, and also implies that a microlayer is likely trapped on the solid

surface (Cooper & Lloyd 1969; Hänsch & Walker 2016). We use R_b to denote the bubble's time-dependent hemispherical cap radius. The vapour in the bubble is at saturation with a uniform pressure p_v. The surrounding liquid is at a constant saturation state, characterised by a pressure p_∞.

Our focus here is on the early stage of microlayer deposition by the expanding bubble, i.e. the hydrodynamic aspects of the microlayer. The phase change effect becomes apparent after the creation of the microlayer. Experimental observations have highlighted the thinning of the microlayer due to mass loss through evaporation, indicating that the microlayer creation is a faster process than evaporation. For instance, the microlayer is formed within 1 ms for water at atmospheric pressure, whereas the time scales associated with the liquid evaporation are at least one order of magnitude larger (Utaka, Kashiwabara & Ozaki 2013; Chen *et al.* 2020). Therefore, it is possible to describe the microlayer formation from a pure hydrodynamic perspective.

The thickness of this microlayer is typically two to three orders of magnitude smaller than its radial extension, $\delta/R_b \ll 1$; e.g. for water boiling at atmospheric pressure, the microlayer reaches thicknesses of a few micrometres, while its radial extension is of the order of 1 mm. Therefore, in this work, the evolution of this microlayer is described using the lubrication approximation. For $r \to 0$, the film terminates with a triple solid–liquid–vapour contact line, which leaves a dry patch centred at $r = 0$. As $r \to \infty$, the microlayer profile joins the advancing bubble front at the bottom of the hemispherical cap of the bubble.

The microlayer can be divided into three distinct regions along the radial direction; see figure 1(*a*). The first (innermost) region is near the triple contact line. We consider a highly wettable solid surface to facilitate microlayer formation (Bureš & Sato 2021). The contact line receding is slow on wettable surfaces due to the small contact angle (Snoeijer & Eggers 2010; Zhang & Nikolayev 2022), thus its motion can be neglected during microlayer formation. After this phase, the expanding dry area may give rise to a dewetting ridge (Urbano *et al.* 2018; Tecchio *et al.* 2022). However, this dewetting effect is out of the scope of this study. The second region is a thin layer of liquid, where the interface is nearly parallel to the solid surface, described in § 2.1 using the lubrication approximation. The third region is the bubble front, which takes a meniscus shape, described in § 2.2. The interface transitions from the nearly flat microlayer to the nearly hemispherical bubble dome of radius R_b. We refer to the outermost part of the interface as the 'bubble front', identified by the radial position r_f, where r_f also represents the width of the bubble, under the hemispherical assumption $r_f \approx R_b$. At the point of the interface transitioning between the last two regions, there exists a meniscus with the characteristic radius of curvature R_m (Smirnov 1975; Zijl & Moalem-Maron 1978). This meniscus marks the outer edge of the microlayer and is responsible for determining the thickness of the deposited liquid film on the solid. We denote its outward-moving speed as u_m. The speed u_m can be approximated as the bubble expansion rate $\dot{R}_b(t)$.

2.1. *Equations for the thin film region*

To emphasise the similarity of this problem with the Landau–Levich film (Landau & Levich 1942), we change the axisymmetric coordinate system (r, z) to a planar coordinate system (x, z), in a frame of reference moving with the bubble front r_f; see figure 1(*b*), where $x = -r + r_f$. The assumption of planar flow is justified by the slender nature of the microlayer with a thickness two orders of magnitude smaller than its radial extension r. In such a frame of reference, the solid wall is pulling up at speed u_m with respect to

the liquid bath, and a thin layer of liquid is deposited on it. Landau & Levich (1942) studied the problem of an infinite flat film. If the contact line is present, then when the film length is significantly larger than the thickness of the liquid film, Snoeijer *et al.* (2006) has shown that the liquid film far from the contact line can still be described as the original Landau–Levich problem.

The original theory for determining the thickness of the liquid film was developed under the assumption of a solid moving at a constant speed, implying the static behaviour of the meniscus. The meniscus speed u_m generally decreases as the bubble grows larger, which does not satisfy static conditions. Nevertheless, Zhang & Nikolayev (2021) have demonstrated that the quasi-steady solution remains a valid approximation for dynamic scenarios in which the meniscus speed and curvature vary over time. It is shown that thin liquid films deposited on the inner walls of capillary tubes by receding menisci of liquid plugs remain nearly stationary after deposition due to high viscosity in the thin film if phase change is absent. A similar behaviour is expected for the microlayer. The initial thickness at a radial distance r is determined by the speed u_m and R_m at the instant when the meniscus passes through r (Zhang & Nikolayev 2021).

For the thin film region in figure 1(*b*), Landau and Levich derived an equation describing the thickness δ using the lubrication theory:

$$\frac{\partial^3 \delta}{\partial x^3} = \frac{3\mu u_m}{\sigma} \frac{\delta_{0,LL} - \delta}{\delta^3}, \tag{2.1}$$

where μ is the liquid viscosity, and σ is surface tension. Unless otherwise indicated, all quantities used refer to the liquid phase. Here, $\delta_{0,LL}$ is the asymptotic liquid film thickness far from the meniscus region, where the interface tends to be parallel to the solid wall.

This is the upper boundary condition to (2.1):

$$\delta \to \delta_{0,LL}, \quad \frac{\partial \delta}{\partial x} \to 0 \quad \text{and} \quad \frac{\partial^2 \delta}{\partial x^2} \to 0, \quad \text{as } x \to \infty. \tag{2.2}$$

'Upper' refers to the relative direction indicated in figure 1(*b*). The lower boundary conditions are presented in § 2.3.

2.2. *Equations for the meniscus region*

In the meniscus region, across the curved interface, there is a discontinuity in normal stress that can be expressed by the Laplace equation

$$p(x) = p_v - \sigma K, \tag{2.3}$$

where p is the liquid pressure near the interface, and K is the interface curvature calculated as the total curvature of a shell of revolution around the z-axis in figure 1(*a*) (Bucci 2020):

$$K = K_1 + K_2 = \left[\frac{x}{\sin\left(\tan^{-1}\frac{\partial \delta}{\partial x}\right)} \right]^{-1} + \frac{\dfrac{\partial^2 \delta}{\partial x^2}}{\left[1 + \left(\dfrac{\partial \delta}{\partial x}\right)^2 \right]^{3/2}}, \tag{2.4}$$

where K_1 and K_2 are the parallel and meridian parts of the curvature, respectively. In the meniscus region, the interface slope is large, and K_1 satisfies

$$K_1 \approx \frac{1}{R_b}. \tag{2.5}$$

To obtain the liquid pressure near the interface in the third region, we use the full expression for the interface curvature in (2.4) and use the Rayleigh equation in the differential form (Tong & Tang 2017),

$$\frac{\partial p}{\partial r} = -\rho \left(\frac{2R_b \dot{R}_b^2 + R_b^2 \ddot{R}_b}{r^2} - \frac{2R_b^4 \dot{R}_b^2}{r^5} \right), \tag{2.6a}$$

$$\frac{\partial^2 p}{\partial r^2} = \rho \left(\frac{4R_b \dot{R}_b^2 + 2R_b^2 \ddot{R}_b}{r^3} - \frac{10R_b^4 \dot{R}_b^2}{r^6} \right), \tag{2.6b}$$

where ρ is the density of the liquid. Equations (2.6) represent the liquid pressure gradient outside the interface of a growing bubble R_b in a liquid of infinite extent. Constant liquid pressure p_∞ is reached as $r \to \infty$.

Using (2.6), we approximate the liquid pressure near the interface as

$$p(r) \approx p(R_b) + (r - R_b) \left. \frac{\partial p}{\partial r} \right|_{r=R_b} + \frac{1}{2}(r - R_b)^2 \left. \frac{\partial^2 p}{\partial r^2} \right|_{r=R_b}. \tag{2.7}$$

Substituting the pressure derivatives using (2.6) results in

$$p(r) \approx p(R_b) - \rho \ddot{R}_b (r - R_b) - \rho \left[3 \left(\frac{\dot{R}_b}{R_b} \right)^2 - \frac{\ddot{R}_b}{R_b} \right] (r - R_b)^2. \tag{2.8}$$

Strictly speaking, (2.8) is applicable to the liquid outside the hemispherical interface. Regardless, we make the approximation of extending its application to the liquid area close to, but inside, the extension of the hemispherical interface (as depicted in the dashed region in figure 1(a)). This area is sufficiently distant from the solid surface, making boundary layer effects negligible. Taking (2.8) back to the frame of reference of the moving meniscus as in figure 1(b), and using $x = -r + r_f$, leads to

$$p(x) \approx p(R_b) + \rho \ddot{R}_b x - \rho \left[3 \left(\frac{\dot{R}_b}{R_b} \right)^2 - \frac{\ddot{R}_b}{R_b} \right] x^2, \tag{2.9}$$

where x is positive, representing the liquid pressure near the interface in the dashed area.

Incorporating the viscosity effect of bubble expansion and accounting for the usual discontinuity in normal stress, the pressure drop across the interface is given as (Tong & Tang 2017)

$$p(R_b) = p_v - \frac{2\sigma}{R_b} - 4\mu \frac{\dot{R}_b}{R_b}, \tag{2.10}$$

where the second and third terms on the right-hand side represent the contributions of surface tension and viscosity, respectively. To assess the relative importance of these two terms, we calculate the ratio of the viscous term to the surface tension term, and obtain $2\mu \dot{R}_b / \sigma = 2\,Ca_b \sim 10^{-2}$, where Ca_b represents the capillary number of bubble growth. Since the ratio is small, the viscous effect on the pressure discontinuity across the interface will be omitted from further consideration.

Substituting (2.10) into (2.9) and then equating the obtained expression to (2.3), we find the equation for the dynamic meniscus in the transition region as

$$
\frac{\dfrac{\partial^2 \delta}{\partial x^2}}{\left[1 + \left(\dfrac{\partial \delta}{\partial x}\right)^2\right]^{3/2}} = \frac{\rho}{\sigma}\left[3\left(\frac{\dot{R}_b}{R_b}\right)^2 - \frac{\ddot{R}_b}{R_b}\right]x^2 - \frac{\rho \ddot{R}_b}{\sigma}x + \frac{1}{R_b}. \tag{2.11}
$$

We integrate (2.11) in the interval $[0, x]$, which produces

$$
\frac{\dfrac{\partial \delta}{\partial x}}{\left[1 + \left(\dfrac{\partial \delta}{\partial x}\right)^2\right]^{1/2}} = \frac{\rho}{\sigma}\left[\left(\frac{\dot{R}_b}{R_b}\right)^2 - \frac{\ddot{R}_b}{3R_b}\right]x^3 - \frac{\rho \ddot{R}_b}{2\sigma}x^2 + \frac{1}{R_b}x - 1, \tag{2.12}
$$

where the constant -1 on the right-hand side is determined using the condition $\partial \delta/\partial x \to -\infty$ at $x \to 0$, i.e. the interface is nearly perpendicular to the solid surface. Equations (2.11) and (2.12) determine the thickness of the liquid δ in the meniscus region close to the bubble front.

2.3. *Matching the thin film and meniscus regions*

We first look at the meniscus region. At small values of δ, the solution of (2.11) and (2.12) must go over into the solution for the thin film region, which is governed by (2.1). Therefore, using the limit of small δ, we have $\partial \delta/\partial x \to 0$ in the solution of the meniscus region. At the same time, the left-hand side of (2.12) approaches 0, and x approaches a value denoted as $\bar{x}$. Its value is the positive root of the equation

$$
a_3 x^3 + a_2 x^2 + a_1 x + a_0 = 0, \tag{2.13}
$$

where

$$
a_3 = \frac{\rho}{\sigma}\left[\left(\frac{\dot{R}_b}{R_b}\right)^2 - \frac{\ddot{R}_b}{3R_b}\right], \quad a_2 = -\frac{\rho \ddot{R}_b}{2\sigma}, \quad a_1 = \frac{1}{R_b}, \quad a_0 = -1. \tag{2.14}
$$

Note that $\bar{x} = \sqrt{2\sigma/(\rho g)}$ is the characteristic length in the Landau–Levich original formulation (Landau & Levich 1942).

The law of growth for R_b is commonly expressed as $R_b = C_b t^n$, where C_b is a constant determined by the heating conditions and the properties of the liquid. For bubbles on solid surfaces during the thermal diffusion controlled stage, the value of n is given theoretically as 0.5 by Mikic *et al.* (1970), whilst in some experiments, $n < 0.5$ is reported (Sinha *et al.* 2022). The second time derivative $\ddot{R}_b = n(n-1)C_b t^{n-2}$ remains negative regardless. Consequently, the coefficients a_3, a_2 and a_1 are positive, and (2.13) possesses a single positive root.

With the help of (2.11), we find that the second derivative of δ at $x = \bar{x}$ tends to

$$
\left.\frac{\partial^2 \delta}{\partial x^2}\right|_{x=\bar{x}} = 3a_3\bar{x}^2 + 2a_2\bar{x} + a_1, \tag{2.15}
$$

which indicates that the meniscus region has a constant value of $\partial^2 \delta/\partial x^2$ as the upper limit of the region.

997 A44-8

The lower limit of the thin film region corresponds to the upper limit of the meniscus region, thus for matching the two solutions, we require the continuity of the second derivative $\partial^2 \delta / \partial x^2$ as in Landau & Levich (1942). Equation (2.15) provides the sought lower boundary condition required for the solution of (2.1). Recall that the lubrication theory is applied to the thin film region, therefore the continuity of $\partial^2 \delta / \partial x^2$ indicates the continuity of the interface curvature as $\partial \delta / \partial x$ is small in this region. The constant identified at the right-hand side of (2.15) coincides with the curvature of the interface $1/R_m$, thus the lower boundary condition for (2.1) can be rewritten as

$$\left. \frac{\partial^2 \delta}{\partial x^2} \right|_{\delta \to \infty} \to \frac{1}{R_m}, \tag{2.16}$$

where R_m is the radius of the characteristic curvature in the meniscus region, as illustrated in figure 1(a). Landau and Levich decided this matching point at $\bar{x}$, and the matching condition requires

$$\frac{1}{R_m} = \left. \frac{\partial^2 \delta}{\partial x^2} \right|_{x=\bar{x}}. \tag{2.17}$$

Therefore, (2.16) and (2.17) provide the lower boundary conditions to (2.1). With the help of both upper and lower boundaries, a numerical solution to (2.1) has been given (Landau & Levich 1942) as

$$\delta_0 \approx 1.34 R_m \left(\frac{\mu u_m}{\sigma} \right)^{2/3}, \tag{2.18}$$

where the upper boundary condition $\delta_{0,LL}$ is replaced with δ_0 as we determine the initial microlayer thickness as a Landau–Levich film. In this equation, R_m is calculated using (2.17) and (2.15), and u_m can be equal to $\dot{R}_b$ approximately. The coefficient 1.34 in the equation was obtained numerically by Landau and Levich under the condition that $\mu u_m / \sigma$ is sufficiently small. This condition is generally satisfied as $\dot{R}_b \ll \sigma / \mu$ for a given fluid.

Equation (2.18) suggests that microlayer formation should result from a balance between surface tension, viscosity and inertial effects. While the above analysis applies the lubrication approximation and does not explicitly consider inertial effects, they play a significant role in the overall dynamics of bubble growth. The inertial effects impact the second time derivative of R_b. This, in turn, influences the value of R_m in the meniscus region. Our analysis maintains well-defined surface tension, with no shear stress applied to the interface. Factors like liquid impurities, surfactants and highly curved interfaces, which could lead to variations in interface temperature and non-uniform surface tension, are not taken into account.

Compared to the theory of determining the microlayer thickness as the displacement thickness of the hydrodynamic boundary layer outside the bubble on the solid (Cooper & Lloyd 1969; Olander & Watts 1969), (2.18) incorporates the effect of surface tension and regards the formation of the microlayer as a local phenomenon due to the liquid flow near the bubble front. Notably, obtaining this equation is independent of the common assumption of the growth law as $R_b \propto t^{0.5}$, which indicates that the equation can handle complex bubble growth patterns.

We must also notice that the derivation of (2.18) assumes the formation of the microlayer on smooth surfaces. In reality, given that δ_0 is typically of the order of a few micrometres, which can be close to the surface roughness, additional corrections may be necessary for surfaces with an absolute roughness of the order of $1 \, \mu m$.

3. Validation and discussion

This section compares the prediction of (2.18) with experimental data on the initial microlayer thickness, and discusses some characteristics of the microlayer using the proposed model.

3.1. *Experiments by Jung & Kim (2018)*

Jung & Kim (2018) conducted experiments on single bubble nucleate boiling in a pool of saturated water under atmospheric pressure. The fluid properties of saturated water and steam (Harvey 1998) are summarised in table 1. Their experiment observed the growth of a bubble on an indium tin oxide (ITO) coated heater, driven by phase change. A high-speed camera captured the bubble growth, and $R_b(t)$ was reported as plotted in figure 2. A microlayer was observed on the ITO surface, and its thickness was measured using laser interferometry. Due to the heat applied by the heater, liquid evaporated from the microlayer, resulting in a thinning of the microlayer. To account for this mass loss, they reconstructed the initial thickness of the microlayer $\delta_0(r)$ when it was initially deposited on the ITO surface, utilising the heater temperature data.

We established a power regression fitting curve for the Jung & Kim (2018) data for $R_b(t)$ as

$$R_b(t) \approx 0.0455t^{0.5}, \tag{3.1}$$

which provides the growth rate $\dot{R}_b$ plotted in figure 2.

At each time instant, coefficients a_3, a_2 and a_1 are calculated as indicated in (2.14), using known values of $\dot{R}_b$ and $\ddot{R}_b$. The value of $\bar{x}$ is then found by solving (2.13), and the corresponding R_m is plotted in figure 2. When calculating δ_0 using (2.18), we assume that the velocity of the bubble front is equal to the bubble growth rate: $u_m = \dot{R}_b$. For an adequate comparison, we also compute the predictions of (1.1) by Cooper & Lloyd (1969) with $C = 0.8$, (1.2) by Smirnov (1975), and (1.3) by Zijl & Moalem-Maron (1978).

Figure 3 presents a comparison of predictions for the initial microlayer thickness as a function of radial distance r based on (1.1), (1.2), (1.3) and (2.18). It is assumed that the thickness at a position r is determined by the instant where the meniscus passes through. The initial thickness reconstructed from experimental measurements by Jung & Kim (2018) is also included in the plot for comparison. The microlayer thickness exhibits a consistent, monotonic increase from the nucleation site and remains below $6\,\mu$m in the experimental data, which is in good agreement with the prediction of the proposed model (2.18). Despite the steady decrease in the bubble's growth rate, denoted as $\dot{R}_b$ or u_m, the radius of curvature R_m continues to increase with R_b, surpassing the reduction in $\dot{R}_b$. This results in δ_0, a product of R_m and u_m, showing a rising trend. Notably, the predictions from (1.1) and (1.2) tend to overestimate the microlayer thickness by over 200 %.

3.2. *Experiments by Sinha et al. (2022)*

Sinha *et al.* (2022) investigated bubble behaviour and microlayer dynamics during the growth of a single bubble on the heated solid wall of a vertical rectangular flow channel. The experiments were conducted with sub-cooled water under atmospheric pressure conditions. In the early rapid growth stage, both the bubble and microlayer exhibited symmetric expansion in the flow direction and perpendicular to the bulk flow, which led to the conclusion that the impact of bulk flow during the early stage was negligible, and the bubble growth process resembled that characteristic of pool boiling conditions. The thin-film interferometry technique, coupled with high-speed cinematography, captured the

	Density ρ (kg m^{-3})	Dynamic viscosity μ (Pa s)	Conductivity k (W K^{-1} m^{-1})	Heat capacity c_p (J kg^{-1} K^{-1})	Surface tension σ (N m^{-1})	Latent heat $\mathcal{L}$ (J kg^{-1})	Thermal expansion β (K^{-1})
Water	958	2.82×10^{-4}	0.677	4216	0.058	2.256×10^{6}	7.52×10^{-4}
Steam	0.597	1.23×10^{-5}	0.024	2034	—	—	—
Ethanol	757	4.29×10^{-4}	0.154	3000	0.0177	9.63×10^{5}	1.41×10^{-3}
Ethanol vapour	1.435	1.04×10^{-5}	0.02	1830	—	—	—

Table 1. Fluid properties of saturated water ($T_{sat} = 373.15$ K) and ethanol ($T_{sat} = 351.4$ K) at atmospheric pressure.
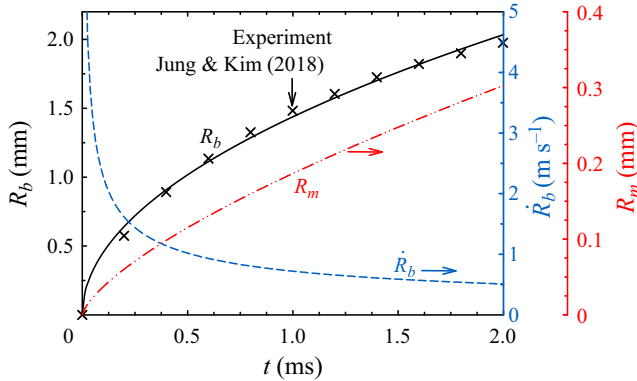
Figure 2. The Jung & Kim (2018) experimental data of bubble radius as a function of time (crosses), the power regression curve (solid line) and the bubble growth rate $\dot{R}_b$ based on the regression curve (blue dashed line). The corresponding R_m calculated by (2.17) is plotted in red.
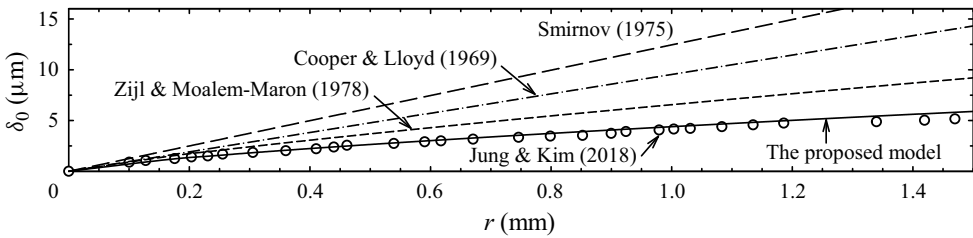

Figure 3. Initial thicknesses of the microlayer reconstructed from experimental data of Jung & Kim (2018) (circles), predicted by the proposed model of (2.18) (solid line), and from Cooper & Lloyd (1969) (dash-dotted line), Smirnov (1975) (long dashed line) and Zijl & Moalem-Maron (1978) (short dashed line).

spatial and temporal evolution of the microlayer thickness. This approach allowed for recording the side view of the bubble as a function of time.

The experimentally recorded equivalent bubble radius $R_b(t)$ for flow Reynolds number $Re = 3600$ is represented by black crosses in figure 4. The growth law $R_b(t) \propto t^{0.5}$ is not suitable for accurately predicting the data in this experiment, as the bulk liquid is sub-cooled. The growth law $R_b(t) \propto t^{0.5}$ was originally developed for bubbles growing in a saturated liquid. Therefore, Sinha *et al.* (2022) used a power regression for the experimental data of $R_b(t)$,

$$R_b(t) \approx 0.01652t^{0.4254}, \tag{3.2}$$

which is plotted as a black solid curve in figure 4. The bubble growth rate $\dot{R}_b(t)$ and R_m calculated by (2.17) are also obtained using the fitting curve of $R_b(t)$.

Assuming $u_m \approx \dot{R}_b(t)$, the predicted initial microlayer thickness δ_0 from (2.18) is compared with the experimental data (circles) in figure 5. Equation (1.1) cannot provide a prediction as the growth law does not follow $R_b(t) \propto t^{0.5}$. Equations (1.2) and (1.3) can still be applied, and their predictions are shown as the long and short dashed lines in figure 5, respectively. Although the two equations are not limited by the assumption $R_b(t) \propto t^{0.5}$, they overestimate the thickness, especially (1.2), as the dashed lines are above the experimental data in figure 5. The proposed model generally yields thickness values that agree with the experimental measurement.
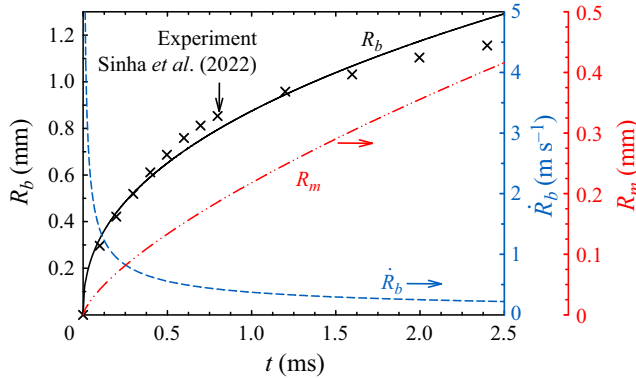
997 A44-12

Figure 4. The Sinha *et al.* (2022) experimental data of bubble radius as a function of time (crosses), the power regression of (3.2) (solid line), and the bubble growth rate $\dot{R}_b$ based on the regression curve (blue dashed line). The corresponding R_m calculated by (2.17) is plotted in red.
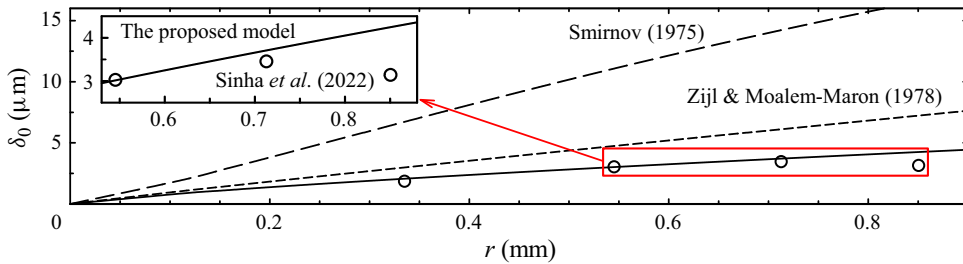

Figure 5. Initial thicknesses of the microlayer: experimental data of Sinha *et al.* (2022) (circles), and predictions by (2.18) (solid line), by Smirnov (1975) (long dashed line) and by Zijl & Moalem-Maron (1978) (short dashed line). The three rightmost data points are enlarged and shown in the inset.

A distinctive feature highlighted in the experiments of Sinha *et al.* (2022) is the reduction in microlayer thickness at its outer periphery, accompanied by a slight curvature in the interface. This characteristic is depicted in the inset of figure 5, where the rightmost data points are magnified for clarity. This non-monotonic behaviour is not captured by the proposed model, which predicts a constantly increasing thickness from the nucleation site. The non-monotonic aspect is addressed in § 3.3.2.

3.3. *Some characteristics of the microlayer*

3.3.1. *Thickness dependence on the bubble growth rate*
Chen *et al.* (2020) conducted nucleate boiling experiments in a water pool under atmospheric pressure, measuring the microlayer thickness through laser interferometry across a wide range of heat fluxes, leading to various bubble growth rates. Their findings suggested a weak dependence of the initial microlayer thickness on the bubble expansion rate. This conclusion aligns with the earlier results obtained by Utaka *et al.* (2013), who conducted similar experiments measuring the microlayer structure in nucleate pool boiling for water and ethanol under atmospheric pressure. Based on their experimental data, Utaka *et al.* (2013) proposed two empirical formulas for predicting the initial microlayer thickness

regardless of the growth rate:

$$\delta_0(r) = 4.46 \times 10^{-3} r, \quad \text{water}, \qquad (3.3a)$$

$$\delta_0(r) = 1.02 \times 10^{-2} r, \quad \text{ethanol}, \qquad (3.3b)$$

where r is in mm, and δ_0 is given in μm.

Yabuki & Nakabeppu (2014) also proposed an empirical formula based on their experiments of boiling bubbles on a heated surface in a pool of saturated water, as

$$\delta_0(r) = 4.34 r^{0.69}, \qquad (3.4)$$

where r is in millimetres, and δ_0 is given in micrometres.

To test this feature of the microlayer, we employ the growth law proposed by Mikic *et al.* (1970) for bubbles growing on a heated surface with temperature T_w:

$$R_b(t) = C_b(\Delta T) t^{0.5}, \qquad (3.5)$$

where $C_b(\Delta T) = 2\sqrt{3/\pi}\, Ja \sqrt{\alpha}$ is the growth constant related to the solid superheat, $\Delta T = T_w - T_{sat}$, T_{sat} is the saturation temperature of the liquid corresponding to the liquid pool pressure p_∞, and $\alpha = k/(\rho c_p)$ is the thermal diffusivity. The Jakob number Ja is defined as

$$Ja = \frac{\rho c_p (T_w - T_{sat})}{\rho_v \mathcal{L}}, \qquad (3.6)$$

where c_p is the heat capacity of the liquid, ρ_v is the density of the vapour, and $\mathcal{L}$ is the latent heat. Various bubble growth rates are achieved by tuning ΔT.

Equation (3.5) is employed to describe the bubble growth during the diffusion-controlled stage on superheated solid surfaces in a uniformly saturated liquid. We disregard the initial inertia-controlled growth, typically occurring within a duration shorter than 0.1 ms (Mikic *et al.* 1970). Two distinct superheat conditions are considered, with $\Delta T = 10$ K and 25 K, assuming that the bubble growth on the solid surface adheres to (3.5) and that its interface is nearly hemispherical, implying $u_m \approx \dot{R}_b$. The microlayer thickness δ_0, predicted by (2.18), is computed and plotted against the radial distance from the nucleate site r in figure 6. The experimentally obtained (3.3) and (3.4) are presented in the same plot. The fluid properties of saturated water and ethanol at atmospheric pressure are listed in table 1.

The prediction of the initial microlayer thickness by the present model is in good agreement with the empirical relations (3.3) and (3.4). The variation in microlayer thickness exhibits weak dependence on the change in the superheat conditions. For water, the growth rates are $C_b(10\,\text{K}) \approx 2.4 \times 10^{-2}\,\text{m s}^{-0.5}$ and $C_b(25\,\text{K}) \approx 6.0 \times 10^{-2}\,\text{m s}^{-0.5}$. For ethanol, the growth rates are $C_b(10\,\text{K}) \approx 8.4 \times 10^{-3}\,\text{m s}^{-0.5}$ and $C_b(25\,\text{K}) \approx 2.1 \times 10^{-2}\,\text{m s}^{-0.5}$. Despite a 2.5-fold alteration in the growth rate, the corresponding change in δ_0 is less than 20 %. This observation aligns with experimental findings, confirming that the initial microlayer thickness demonstrates little sensitivity to heat flux, i.e. to the bubble expansion rate (Utaka *et al.* 2013; Chen *et al.* 2020). The present model also predicts that the microlayer thickness of ethanol is about 1.5 larger than that of water at the same r. This is also in agreement with experimental observations (Koffman & Plesset 1983).

3.3.2. *Spatial variation of the interface profile*

In the preceding subsection, we used the assumption of $R_b(t) \propto t^{0.5}$, a common feature in multiple theories that predict the microlayer thickness. The resultant spatial profile of the microlayer exhibits a steady increase from the nucleation site. This wedge-like microlayer
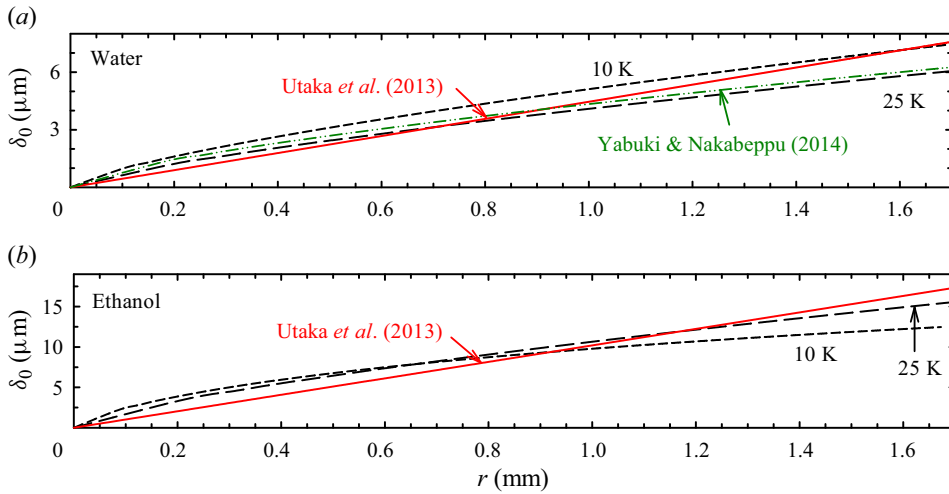
(*a*)

(*b*)

Figure 6. Comparison of the initial microlayer thickness predicted by the present model and empirical formulas of Utaka *et al.* (2013) and Yabuki & Nakabeppu (2014): (*a*) water, (*b*) ethanol.

structure aligns with observations from many experiments (Utaka *et al.* 2013; Jung & Kim 2014, 2018; Chen *et al.* 2020).

A non-monotonic profile of microlayer thickness has also been reported: it reaches a plateau in the middle, then decreases towards the outer edge of the meniscus, resembling an interface bent like a speed bump with a local maximal thickness (Chen *et al.* 2017; Sinha *et al.* 2022; Tecchio *et al.* 2022). This distinctive pattern mirrors the film deposited by a meniscus travelling at non-constant speeds in capillary tubes, a phenomenon observed experimentally by Youn *et al.* (2016) and Youn, Han & Shikazono (2018), and explained theoretically by Zhang & Nikolayev (2021) using the Landau–Levich film problem under unsteady conditions. As depicted in (2.18), the thickness results from the product of the radius of curvature of the meniscus and its advancing speed. Throughout the entire process of a bubble growing on solid surfaces, the bubble undergoes expansion at a decelerating rate: R_b increases monotonically with time, yet $\ddot{R}_b$ is negative. In the later stages of bubble growth, the microlayer's width nearly halts expansion on the solid, and the expansion speed approaches zero. Consequently, the resulting thickness calculated by (2.18) could decrease, suggesting the possibility of a maximal thickness during the process.

Moreover, in real-world scenarios, the values of $R_b(t)$ and the bubble's width on the solid should eventually approach a maximal value, in contrast to the implication of the proportionality law $R_b(t) \propto t^n$, which suggests an indefinite growth of $R_b(t)$. This highlights the need for a more nuanced model that accounts for the eventual stabilisation of these parameters at later stages. To address this, we propose a function

$$R_b(t) = R_c - (R_c - C_b t^n)\, \mathrm{e}^{-t/t_c}, \tag{3.7}$$

where R_c represents the radius towards which the bubble approaches the end stage of growth, and t_c characterises the rate at which the bubble approaches R_c. For small t, this function approximates $R_b(t) \approx C_b t^n$, implying adherence to the power growth law that can be determined as in (3.5). As t approaches t_c, $R_b(t) \approx R_c$, indicating that the bubble is close to a non-growth stage. This construction more accurately reflects real-world situations, providing a more realistic representation of bubble growth dynamics.
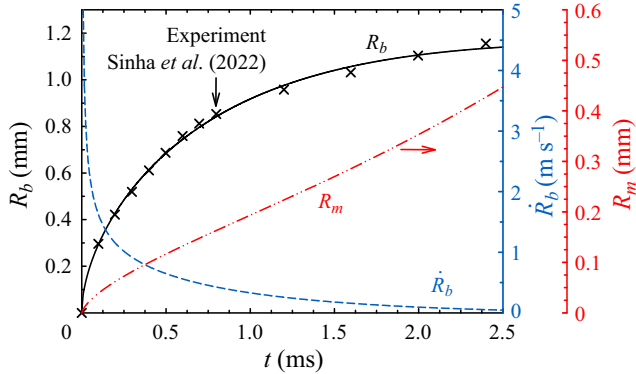
Figure 7. The Sinha *et al.* (2022) experimental data of bubble radius as a function of time (crosses), the regression of (3.7) (solid line), and the bubble growth rate $\dot{R}_b$ based on the regression curve (blue dashed line). The corresponding R_m calculated by (2.17) is plotted in red.
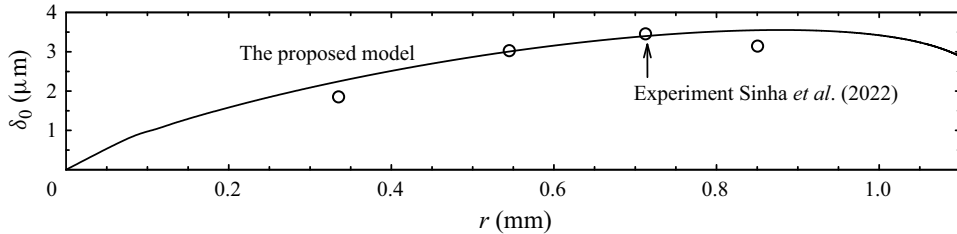

Figure 8. Initial thicknesses of the microlayer: experimental data of Sinha *et al.* (2022) (circles), and prediction by (2.18) (solid line) using (3.7) to describe the bubble growth rate.

The experimental data of $R_b(t)$ by Sinha *et al.* (2022) are employed to determine the parameters in (3.7). The regression curve is depicted in figure 7, with $R_c = 1.10 \times 10^{-3}$ m, $C_b = 2.58 \times 10^{-2}$ m s$^{-0.5}$, $n = 0.5$ and $t_c = 1.96 \times 10^{-3}$ s. Compared with the regression curve for R_b in figure 4, (3.7) aligns more closely with the experimental data, particularly for larger t. Using the new regression curve, (2.18) is employed to compute the microlayer thickness as a function of r. The results are plotted and compared in figure 8. The slight change in the behaviour of R_b results in a noticeable alteration in the microlayer profile: the thickness no longer exhibits a monotonic increase, but instead features a maximal value before decreasing. The resulting profile shows an outward curvature, resembling the observations made by Sinha *et al.* (2022).

We consider another simplified scenario to highlight the expansion deceleration effect on the microlayer profile. We construct two laws of growth using (3.5) and (3.7), setting $C_b = 3 \times 10^{-2}$ m s$^{-0.5}$ in both equations. We introduce a minor deceleration effect by setting $R_c = 9.5 \times 10^{-4}$ m and $t_c = 3 \times 10^{-3}$ s in (3.7). Consequently, for small t, the bubble growth of both equations closely follows the power law, while for larger t, the growth decelerates as specified in (3.7), where R_b approaches R_c. The respective bubble radii as functions of time, specified by the two growth laws, are illustrated in figure 9. The corresponding bubble growth rates $\dot{R}_b$ and R_m, calculated using (2.17), are also depicted. As expected, $\dot{R}_b$ exhibits a lower rate for the growth law of (3.7) when t is large. By applying these growth laws, we can calculate the initial thickness of the microlayer as predicted by the model. The results are presented in figure 10. At small r (i.e. short t), the
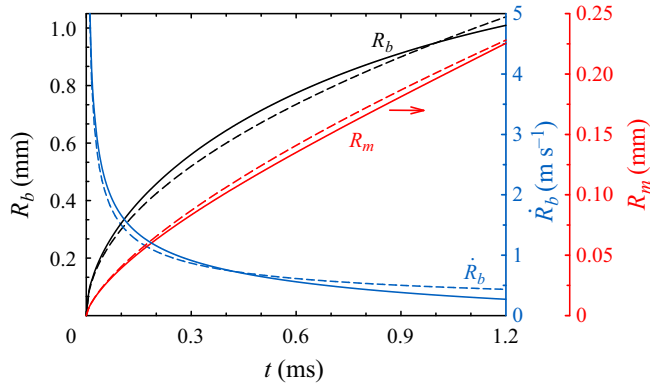
997 A44-16

Figure 9. Comparison of the two laws of growth for the bubble radius R_b: unstopped as specified by (3.5) (dashed lines) and subsiding as calculated by (3.7) (solid lines). The bubble growth rates $\dot{R}_b$ are plotted in blue, and the corresponding R_m calculated by (2.17) are plotted in red.
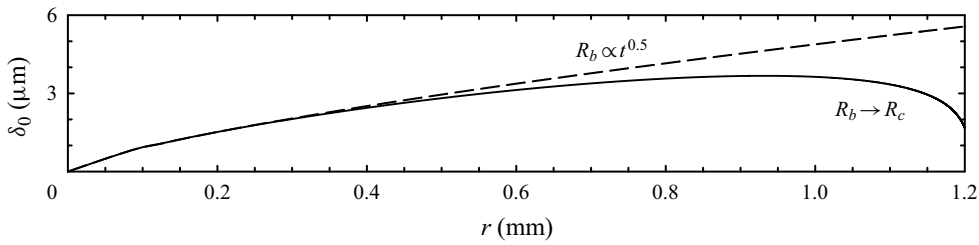

Figure 10. Initial thicknesses of the microlayer predicted by the proposed model using the laws of growth of (3.5) (dashed line) and (3.7) (solid line).

microlayer thicknesses are comparable. However, for larger r, the microlayer thickness for the bubble growth specified by the unstopped growth law of (3.5) continues to increase, while the growth governed by (3.7) reaches a plateau before decreasing. This behaviour illustrates a bent overall interface profile. It is noteworthy that although the two growth laws for R_b in figure 9 almost overlap, with their difference likely being comparable to the experimental uncertainty in the bubble volume measurement, the resulting microlayer thicknesses may differ by up to 30 % at its outer periphery ($r = 1$ mm).

The objective of comparing the two growth laws is to attribute the curved interface profile of the microlayer to the deceleration effect in the expansion rate of the microlayer's outer edge, which is assumed to be equal to the bubble's expansion rate on the solid in the current formulation. Under idealised conditions where the bulk liquid is perfectly superheated, the bubble radius on the solid as a function of time may indeed follow the power law described by (3.5) for an extended period of time. Consequently, the initial thickness of the microlayer would exhibit continuous, non-stop growth from the nucleation site. This scenario might be the case presented in § 3.1, where $R_b(t)$ was well-fitted by (3.5) in figure 2, and a wedge-like profile was observed. The deceleration effect becomes more pronounced when the bulk liquid is sub-cooled or only at saturation. In such cases, the bubble can maintain a fast growth rate at an early stage while it stays in the superheated thermal boundary layer on the solid surface. As the bubble grows taller, it protrudes out of the thermal boundary layer and comes into contact with the sub-cooled liquid; a significant reduction in the growth rate occurs, as the heat transfer from the interface becomes insufficient to sustain the earlier growth rate. The thermal boundary thickness δ_t

on a heated wall in a liquid pool can be calculated as (Kays, Crawford & Weigand 2004)

$$\delta_t \approx 7.14 \left(\frac{\mu\alpha}{\rho g \beta \, \Delta T} \right)^{1/3}, \qquad (3.8)$$

where β is the thermal expansion coefficient of the liquid, and g is the gravitational acceleration. For water on a solid wall superheated by 10 K, $\delta_t \approx 0.62$ mm, which can be smaller than the bubble radius.

Another factor affecting the bubble's expansion on the solid surface is buoyancy, which tends to lift the bubble away from the surface. This effect becomes more pronounced as the bubble grows larger and contributes to the deviation of the bubble from a hemispherical shape (Zhang *et al.* 2024).

We must underline that we refrain from asserting that (3.7) is the definitive or exclusive function to describe the behaviour of $R_b(t)$. Instead, we emphasise that (3.7) serves as one possible simple expression that accounts for the observed slowing-down effect in the radius of vapour bubbles during the later stages of growth on heated solid surfaces. This phenomenon is commonly encountered in practice, contrasting with the idealised proportionality law $R_b(t) \propto t^n$, which implies non-stop bubble expansion.

Another noteworthy observation pertains to the situation when the meniscus reaches its maximum width, at which u_m approaches 0. According to the prediction from (2.18), the thickness then becomes 0. This would impact only a small portion of the thickness prediction. A comparable phenomenon is observed in the meniscus oscillation in capillary tubes. When the meniscus speed decelerates to zero during the deposition of a liquid film, the film thickness decreases but does not reach zero when the meniscus speed decreases to zero (Youn *et al.* 2018; Zhang & Nikolayev 2021). The liquid film remains attached to the meniscus, and so does the microlayer.

4. Conclusions

We propose a phenomenological model that estimates the initial thickness of the microlayer forming under vapour bubbles growing on solid surfaces. This model conceptualises the microlayer as analogous to the liquid film in the Landau–Levich problem. In this framework, the microlayer formation is governed by the liquid flow near the bubble front of the bubble on the solid, and its thickness is determined by the balance of surface tension and viscous forces. Our model offers a broader range of applications, unlike the previous theories relying on specific bubble growth laws as $R_b(t) \propto t^{0.5}$.

We employ the model to compute microlayer thickness under water and ethanol bubbles growing under varying conditions. The comparisons with experimental data have shown good agreement. Considering the idealised growth law for bubbles $R_b(t) = C_b t^{0.5}$, the model predicts that microlayer thickness is insensitive to the growth coefficient C_b, which is associated with the solid's heating flux or, more broadly, the heating conditions of the solid. This observation agrees with previous experimental findings, where the microlayer under water vapour bubbles typically measures below 5 μm at extension 1 mm from the nucleation site, regardless of the heating conditions.

Later, we use the model to investigate the interface profile of the microlayer, addressing inconsistent reports in previous studies. Some reported a wedge-like microlayer with thickness steadily increasing from the nucleation site. Others reported a slightly outwardly curved profile, reaching maximal thickness in the middle, and tapering towards the outermost part of the microlayer. We attribute the decrease in microlayer thickness to the slowing down of the microlayer expansion rate. This is often linked to the deceleration of

the bubble growth rate as the bubble reaches its maximum width on the solid surface. In situations where the microlayer can expand on the solid with the bubble unconstrained, the microlayer thickness will continue to increase constantly. In real-world situations where the bubble experiences a significant reduction in growth rate near its maximal width, the microlayer thickness decreases accordingly. This explains the observed thinner microlayer near the outermost part when the growth slows down compared to earlier stages.

Knowledge of microlayer features from the model can contribute to developing mechanistic models for nucleate boiling heat transfer. Those models require accurate information on the microlayer thickness and growth behaviour as the evaporative heat flux through the microlayer is believed to influence total boiling heat transfer significantly.

Author ORCIDs.
 Xiaolong Zhang (张晓龙) https://orcid.org/0000-0002-7920-3876;
 Ismail El Mellas https://orcid.org/0009-0008-5011-1987;
 Mirco Magnini https://orcid.org/0000-0002-9481-064X.

Appendix A. Comments on Cooper & Lloyd (1969)

Cooper & Lloyd (1969) proposed a simplified hydrodynamic theory that predicts the initial thickness of the microlayer as the displacement thickness of the boundary layer outside a growing bubble. The flow is assumed to be two-dimensional.

The flow pattern in region A (well outside the bubble) is sketched in figure 11(*a*). The liquid velocity reduces from a uniform outward radial velocity to zero in a boundary layer near the wall. The liquid in the microlayer near the bubble front (region C) is not stationary, whilst the velocity decays rapidly in a time of the order of $\delta^2/4\nu$. In region D, the liquid away from the bubble front can be considered at rest.

Obtaining an analytical flow pattern in region B is difficult, as inertial, viscous and surface tension forces are all significant. Cooper & Lloyd (1969) applied a velocity $-u_b$ in the *r*-direction to the flow in figure 11(*a*), which gives the flow pattern sketched in figure 11(*b*) when observed from a reference frame moving with the bubble front: the free interface is nearly stationary, and the liquid velocity $u'(z, t) = u - u_b$ is parallel to the wall. The mass conservation is the major assumption in the original paper, which states that liquid flow from the right-hand side is equal to the rate flowing out at the left-hand side:

$$\delta_0 u_b = \int_0^\infty u' \, \mathrm{d}z, \tag{A1}$$

where the microlayer thickness δ_0 can be regarded as the displacement thickness of the boundary layer in Stokes' first problem, which determines the flow created by a sudden movement of an infinitely long plate to speed u_w from rest. The Navier–Stokes equation
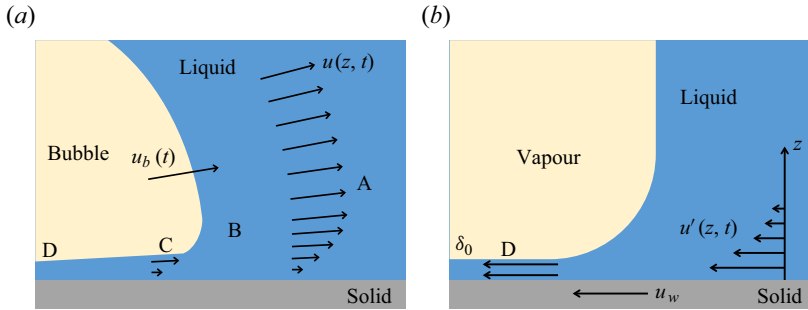
(*a*)   (*b*)

Figure 11. (*a*) Sketch of a growing bubble on the solid and liquid flow. (*b*) Liquid flow pattern in the frame of reference of the moving wall, where the latter moves at a speed u_w towards the left.

for such a problem is reduced to

$$\frac{\partial u'}{\partial t} = \nu \frac{\partial^2 u'}{\partial z^2} \tag{A2}$$

with boundary conditions

$$u'(z) = 0 \quad \text{when } t = 0, \tag{A3a}$$

$$u'(0) = u_w(r, t) \quad \text{and} \quad u'(\infty) = 0 \quad \text{when } t > 0, \tag{A3b}$$

where the velocity $u_w(r, t)$ of the wall is defined below. When solving (A2), Cooper & Lloyd (1969) used

$$u_w(r, t) = \frac{\dot{V}}{2\pi r^2} = C'(r)\, t^n, \tag{A4}$$

where the bubble volume growth rate was estimated as $\dot{V} = 2\pi C_b^3 n t^{3n-1}$, with the bubble radius calculated as $R_b(t) = C_b t^n$. They took $n = 0.5$ and applied $u_w(r, t) = C'(r)t^{0.5}$ to (A3b). A simple form of u' can then be obtained as

$$u' = u_w \sqrt{\pi}\,\text{ierfc}\left(\frac{z}{2\sqrt{\nu t}}\right), \tag{A5}$$

where ierfc(x) is the integral of the complementary error function ierfc(ξ) from x to ∞. Therefore,

$$\int_0^\infty u'\, \mathrm{d}z = u_w \frac{\sqrt{\pi}}{2} \sqrt{\nu t}. \tag{A6}$$

In substituting (A6) into (A1), Cooper & Lloyd (1969) argued that $u_w = u_b$, and consequently obtained

$$\delta_0 = \frac{\sqrt{\pi}}{2} \sqrt{\nu t}. \tag{A7}$$

However, under the hemispherical bubble approximation, $u_b(t)$ should equal $\dot{R}_b = 0.5 C_b t^{-0.5}$, which is inconsistent with their assumption $u_w \propto t^{0.5}$ made in the boundary condition (A3b).

As a matter of fact, u_w should have the form

$$u_w(r, t) = \frac{R_b^2}{r^2}\, u_b(t) \tag{A8}$$

where $r > R_b$, and when the bubble passes the point in question $r = R_b$, we have $u_w = u_b$.

997 A44-20

Applying (A8) to boundary condition (A3*b*), we obtain (Carslaw & Jaeger 1959)

$$u' = \frac{z}{2\sqrt{\pi\nu}} \int_0^t \frac{u_b(\tau)}{(t-\tau)^{3/2}} \exp\left(\frac{-z^2}{4\nu(t-\tau)}\right) d\tau. \tag{A9}$$

The displacement thickness or the microlayer thickness is then calculated by integrating u' from $z = 0$ to infinity using (A1). Equating the microlayer thickness to the displacement thickness of the viscous boundary layer can be considered reasonable when liquid dynamics in the meniscus region is governed primarily by inertial effects. To estimate the importance of inertia, one can calculate the Bond number (Bo) based on the interface acceleration:

$$Bo = \frac{\Delta\rho \, L^2 \, |a_b|}{\sigma}, \tag{A10}$$

where $\Delta\rho$ is the difference in density between the two phases, L is the characteristic length of the meniscus (of the order of 0.1 mm), and a_b is the acceleration of the bubble interface. The Bond number is smaller than 1 in the meniscus region, which indicates that the surface tension effect should not be neglected, and using the displacement thickness would lead to an overestimation of the microlayer thickness.

Appendix B. Review of Smirnov (1975)

Smirnov performed a hydrodynamic analysis of the microlayer in the two-dimensional axisymmetric cylindrical coordinates with simplifications from the lubrication theory. After a meticulous re-examination of his paper, we have found that his formulation contains flawed physical assumptions and derivations. We believe that it is important to show these mistakes as Smirnov's theory is popular in microlayer description.

B.1. *Governing equations*

In the lubrication theory, the liquid in the microlayer moves primarily in the r-direction, implying $u_z \ll u_r$. The equation of momentum in two-dimensional axisymmetric cylindrical coordinates was written as

$$\frac{\partial u_r}{\partial t} + u_r \frac{\partial u_r}{\partial r} = -\frac{1}{\rho} \frac{\partial p}{\partial r} + \nu\left(\nabla^2 u_r - \frac{u_r}{r^2}\right), \tag{B1}$$

where

$$\nabla^2 u_r = \frac{1}{r} \frac{\partial u_r}{\partial r} + \frac{\partial^2 u_r}{\partial r^2} + \frac{\partial^2 u_r}{\partial z^2}. \tag{B2}$$

The equation of continuity in the original paper was written as

$$\frac{\partial}{\partial r}(r u_r \delta_0) = 0, \tag{B3}$$

where $u_r(r, z)$ is the liquid velocity in the r-direction, and δ_0 is the initial thickness of the microlayer.

Without considering phase change, and assuming that the interface stands still once created, the correct form of the continuity equation in the microlayer should be written as

(Zhang & Nikolayev 2021)

$$\frac{\partial \Phi(r)}{\partial r} = 0, \tag{B4}$$

where $\Phi(r)$ represents the liquid volumetric flux through the lateral surface of the cylinder in the microlayer at r, which can be expressed as

$$\Phi(r) = 2\pi r \int_0^{\delta_0} u_r \, dz. \tag{B5}$$

The equation of continuity should then be written as

$$\frac{\partial}{\partial r} \left(r \int_0^{\delta_0} u_r \, dz \right) = 0. \tag{B6}$$

B.2. *Boundary conditions*

Smirnov introduced an assumption regarding the profile of $u_r(z)$ at $r = R_b$ by assuming it as a separation of variables, expressed as

$$u_r = \dot{R}_b \frac{z}{\delta_0} f_2(t), \tag{B7}$$

where $f_2(t)$ is a function of time, with $t = 0$ corresponding to the moment where the microlayer is created. At a given position r, when the bubble interface passes through, $t = 0$ and $f_2(0) = 1$. The value of $f_2(t)$ should decay rapidly as the microlayer does not vary with time if evaporation is absent.

Equation (B7) implies a linear variation of $u_r(z)$ from the solid surface to the interface for a given moment $t > 0$. However, this assumption leads to a non-zero velocity gradient at the free interface: $\partial u_r / \partial z \neq 0$ at $z = \delta_0$, indicating the presence of shear stress on the interface. In practice, this assumption does not hold true for liquid–vapour interfaces if the surface tension is assumed constant, where shear stress at the interface is typically non-existent.

Take a step back. Even if we concede that (B7) is reasonable, one substitutes (B7) into (B6) and the equation of continuity becomes

$$\frac{\partial}{\partial r} \left(r \dot{R}_b \delta_0 \right) = 0, \tag{B8}$$

which is inconsistent with the original equation of continuity (B3).

Later, Smirnov used (B3) to obtain

$$\frac{\partial u_r}{\partial r} = -\frac{u_r}{r} - \frac{u_r}{\delta_0} \frac{\partial \delta_0}{\partial r} \tag{B9}$$

and

$$\frac{\partial^2 u_r}{\partial r^2} = \frac{2u_r}{r^2} + \frac{2u_r}{r\delta_0} \frac{\partial \delta_0}{\partial r} + \frac{2u_r}{\delta_0^2} \left(\frac{\partial \delta_0}{\partial r} \right)^2 - \frac{u_r}{\delta_0} \frac{\partial^2 \delta_0}{\partial r^2}. \tag{B10}$$

Smirnov argued that one should examine the equation of momentum only when the microlayer is just created, where $t = 0$, and assumed $\partial r = \partial R_b$. Substituting (B7) into (B1) using (B9) and (B10), then integrating the obtained expression from $z = 0$ to $z = \delta_0$, one arrives at equation (8) of Smirnov (1975). The coefficient of the second term on the left-hand side of equation (8) should be $-2/3$, instead of -2 as stated in the original paper.

During the processing, the integration of $\partial^2 u_r / \partial z^2$ on the right-hand side was performed by Smirnov as

$$\int_0^{\delta_0} \frac{\partial^2 u_r}{\partial z^2} \, \mathrm{d}z = \left. \frac{\partial u_r}{\partial z} \right|_{z=\delta_0} - \left. \frac{\partial u_r}{\partial z} \right|_{z=0} = 0 - \frac{\dot{R}_b}{\delta_0}, \tag{B11}$$

which is inconsistent with the assumed velocity profile (B7).

After the integration, the calculating equation for determining the initial thickness was then expressed as

$$\delta_0 = \sqrt{\frac{2\nu \dot{R}_b}{-\dfrac{2}{\rho} \dfrac{\partial p}{\partial R_b} - \ddot{R}_b + \dfrac{2\dot{R}_b^2}{3R_b}}}, \tag{B12}$$

where p is the pressure in the liquid at the phase interface. It can be calculated using the Rayleigh equation

$$\frac{p - p_\infty}{\rho} = R_b \ddot{R}_b + \frac{3}{2} \dot{R}_b^2. \tag{B13}$$

In equation (11) of the original paper, an additional term $2\sigma/\rho R_b$ was introduced on the right-hand side of (B13) to account for the discontinuity of the normal stress across the phase interface. However, given that p represents the pressure in the liquid, there seems to be no appropriate place for introducing this discontinuity in (B13). This suggests that the surface tension effect should not have been included in the theory in the first place.

B.3. *Liquid pressure gradient*

To obtain the gradient of the liquid pressure $\partial p / \partial R_b$, Smirnov took the time derivative on both sides of (B13) and made the assumption

$$\left. \frac{\partial p}{\partial r} \right|_{r=R_b} = \frac{\partial p}{\partial t} \frac{\partial t}{\partial R_b}. \tag{B14}$$

Estimating the liquid pressure gradient using the substitution of (B14) raises questions about the validity of the approach, a concern that has also been raised by Bureš & Sato (2022).

Recently, Jung & Kim (2018) reintroduced the surface tension effect, which should not have been included, as demonstrated above. Nonetheless, a mistake exists in their formulation. The last term in the denominator of equation (11) in Jung & Kim (2018) is incorrectly expressed as this term must be dimensionless, and as such, it should be represented as

$$\delta_0 = \sqrt{\frac{2\nu t}{9(1-n) + 2\left(\dfrac{1}{n} - 1\right)(n-2) + 0.66n + \dfrac{4\sigma}{\rho C_b^3 n t^{3n-2}}}}, \tag{B15}$$

where the bubble takes the law of growth in the form $R_b = C_b t^n$. This error also appears in Sinha *et al.* (2022), which used the Jung & Kim (2018) formula. One can estimate the surface tension correction, the last term of the denominator on the right-hand side of

(B15), by assuming $n = 0.5$ and $C_b = 3 \times 10^{-2}\,\text{m}\,\text{s}^{-0.5}$. This term is then calculated for water using fluid properties in table 1:

$$\frac{4\sigma}{\rho C_b^3 n t^{3n-2}} \approx 0.0242 t^{0.5}. \tag{B16}$$

For $t = 1\,\text{ms}$, this term gives a correction of approximately 7.65×10^{-4}, which is much smaller than the sum of the rest in the denominator of 2.33 in (B15).

Since the original equation by Smirnov (1975) contains flawed physical assumptions, utilising an equation based on the original one may lead to results that lack physical coherence.

REFERENCES

BUCCI, M. 2020 A theoretical and experimental study of vapor bubble dynamics in separate effect pool boiling conditions. Master's thesis, Università di Pisa.

BUREŠ, L. & SATO, Y. 2021 On the modelling of the transition between contact-line and microlayer evaporation regimes in nucleate boiling. *J. Fluid Mech.* **916**, A53.

BUREŠ, L. & SATO, Y. 2022 Comprehensive simulations of boiling with a resolved microlayer: validation and sensitivity study. *J. Fluid Mech.* **933**, A54.

CAREY, V.P. 2020 *Liquid–Vapor Phase-Change Phenomena: An Introduction to the Thermophysics of Vaporization and Condensation Processes in Heat Transfer Equipment*, 3rd edn. CRC.

CARSLAW, H.S. & JAEGER, J.C. 1959 *Conduction of Heat in Solids*, 2nd edn. Clarendon.

CHEN, Z., HAGINIWA, A. & UTAKA, Y. 2017 Detailed structure of microlayer in nucleate pool boiling for water measured by laser interferometric method. *Intl J. Heat Mass Transfer* **108**, 1285–1291.

CHEN, Z., HU, X., HU, K., UTAKA, Y. & MORI, S. 2020 Measurement of the microlayer characteristics in the whole range of nucleate boiling for water by laser interferometry. *Intl J. Heat Mass Transfer* **146**, 118856.

COOPER, M.G. & LLOYD, A.J.P. 1969 The microlayer in nucleate pool boiling. *Intl J. Heat Mass Transfer* **12** (8), 895–913.

GAO, M., ZHANG, L., CHENG, P. & QUAN, X. 2013 An investigation of microlayer beneath nucleation bubble by laser interferometric method. *Intl J. Heat Mass Transfer* **57** (1), 183–189.

HÄNSCH, S. & WALKER, S. 2016 The hydrodynamics of microlayer formation beneath vapour bubbles. *Intl J. Heat Mass Transfer* **102**, 1282–1292.

HÄNSCH, S. & WALKER, S. 2019 Microlayer formation and depletion beneath growing steam bubbles. *Intl J. Multiphase Flow* **111**, 241–263.

HARVEY, A.H. 1998 Thermodynamic properties of water: tabulation from the IAPWS formulation 1995 for the thermodynamic properties of ordinary water substance for general and scientific use. *Tech. Rep.* NISTIR 5078. National Institute of Standards and Technology.

JUNG, S. & KIM, H. 2014 An experimental method to simultaneously measure the dynamics and heat transfer associated with a single bubble during nucleate boiling on a horizontal surface. *Intl J. Heat Mass Transfer* **73**, 365–375.

JUNG, S. & KIM, H. 2018 Hydrodynamic formation of a microlayer underneath a boiling bubble. *Intl J. Heat Mass Transfer* **120**, 1229–1240.

KATTO, Y. & SHOJI, M. 1970 Principal mechanism of micro-liquid-layer formation on a solid surface with a growing bubble in nucleate boiling. *Intl J. Heat Mass Transfer* **13** (8), 1299–1311.

KAYS, W., CRAWFORD, M. & WEIGAND, B. 2004 *Convective Heat and Mass Transfer*, 4th edn. McGraw-Hill.

KIM, D.E. & SEOK OH, J. 2021 Phase structure and its temporal evolution under growing single vapor bubble. *Phys. Fluids* **33** (12), 121706.

KOFFMAN, L.D. & PLESSET, M.S. 1983 Experimental observations of the microlayer in vapor bubble growth on a heated solid. *Trans. ASME J. Heat Transfer* **105** (3), 625–632.

LANDAU, L. & LEVICH, B. 1942 Dragging of a liquid by a moving plate. *Acta Physicochim. USSR* **17**, 42–54.

MIKIC, B.B., ROHSENOW, W.M. & GRIFFITH, P. 1970 On bubble growth rates. *Intl J. Heat Mass Transfer* **13** (4), 657–666.

MOORE, F.D. & MESLER, R.B. 1961 The measurement of rapid surface temperature fluctuations during nucleate boiling of water. *AIChE J.* **7** (4), 620–624.

OLANDER, R.R. & WATTS, R.G. 1969 An analytical expression of microlayer thickness in nucleate boiling. *Trans. ASME J. Heat Transfer* **91** (1), 178–180.

VAN OUWERKERK, H.J. 1971 The rapid growth of a vapour bubble at a liquid–solid interface. *Intl J. Heat Mass Transfer* **14** (9), 1415–1431.

PLESSET, M.S. & ZWICK, S.A. 1954 The growth of vapor bubbles in superheated liquids. *J. Appl. Phys.* **25** (4), 493–500.

SINHA, G.K., NARAYAN, S. & SRIVASTAVA, A. 2022 Microlayer dynamics during the growth process of a single vapour bubble under subcooled flow boiling conditions. *J. Fluid Mech.* **931**, A23.

SMIRNOV, G.F. 1975 Calculation of the 'initial' thickness of the 'microlayer' during bubble boiling. *J. Engng Phys.* **28** (3), 369–374.

SNOEIJER, J.H., DELON, G., FERMIGIER, M. & ANDREOTTI, B. 2006 Avoided critical behavior in dynamically forced wetting. *Phys. Rev. Lett.* **96** (17), 174504.

SNOEIJER, J.H. & EGGERS, J. 2010 Asymptotic analysis of the dewetting rim. *Phys. Rev.* E **82** (5), 056314.

TECCHIO, C., ZHANG, X., CARITEAU, B., ZALCZER, G., ROCA I CABARROCAS, P., BULKIN, P., CHARLIAC, J., VASSANT, S. & NIKOLAYEV, V. 2022 Microlayer dynamics at bubble growth in boiling. In *Proc. 16th Int. Conf. Heat Transfer Fluid Mech. Thermodynamics (HEFAT-ATE 2022)*, pp. 624–629.

TONG, L.S. & TANG, Y.S. 2017 *Boiling Heat Transfer and Two-Phase Flow*, 2nd edn. Taylor and Francis.

URBANO, A., TANGUY, S., HUBER, G. & COLIN, C. 2018 Direct numerical simulation of nucleate boiling in micro-layer regime. *Intl J. Heat Mass Transfer* **123**, 1128–1137.

UTAKA, Y., HU, K., CHEN, Z. & MOROKUMA, T. 2018 Measurement of contribution of microlayer evaporation applying the microlayer volume change during nucleate pool boiling for water and ethanol. *Intl J. Heat Mass Transfer* **125**, 243–247.

UTAKA, Y., KASHIWABARA, Y. & OZAKI, M. 2013 Microlayer structure in nucleate boiling of water and ethanol at atmospheric pressure. *Intl J. Heat Mass Transfer* **57** (1), 222–230.

YABUKI, T. & NAKABEPPU, O. 2014 Heat transfer mechanisms in isolated bubble boiling of water observed with MEMS sensor. *Intl J. Heat Mass Transfer* **76**, 286–297.

YOUN, Y.J., HAN, Y. & SHIKAZONO, N. 2018 Liquid film thicknesses of oscillating slug flows in a capillary tube. *Intl J. Heat Mass Transfer* **124**, 543–551.

YOUN, Y.J., MURAMATSU, K., HAN, Y. & SHIKAZONO, N. 2016 The effect of bubble deceleration on the liquid film thickness in microtubes. *Intl J. Heat Fluid Flow* **58**, 84–92.

ZHANG, X., EL MELLAS, I. & MAGNINI, M. 2024 Hydrodynamic characteristics of the microlayer under vapour bubbles on solid surfaces. *J. Phys.: Conf. Ser.* **2766** (1), 012142.

ZHANG, X. & NIKOLAYEV, V.S. 2021 Liquid film dynamics with immobile contact line during meniscus oscillation. *J. Fluid Mech.* **923**, A4.

ZHANG, X. & NIKOLAYEV, V.S. 2022 Dewetting acceleration by evaporation. *J. Fluid Mech.* **948**, A49.

ZIJL, W. & MOALEM-MARON, D. 1978 Formation and stability of a liquid microlayer in pool boiling and growth of a dry area. *Chem. Engng Sci.* **33** (10), 1331–1337.